

μ Split: efficient image decomposition for microscopy data

Ashesh

Fondazione Human Technopole

ashesh.ashesh@fht.org

Alexander Krull

University of Birmingham

a.f.f.krull@bham.ac.uk

Moises Di Sante

University of Pavia, Italy

moises.disante@unipv.it

Francesco Silvio Pasqualini

University of Pavia, Italy

francesco.pasqualini@unipv.it

Florian Jug

Fondazione Human Technopole

florian.jug@fht.org

Abstract

Light microscopy is routinely used to look at living cells and biological tissues at sub-cellular resolution. Components of the imaged cells can be highlighted using fluorescent labels, allowing biologists to investigate individual structures of interest. Given the complexity of biological processes, it is typically necessary to look at multiple structures simultaneously, typically via a temporal multiplexing scheme. Still, imaging more than 3 or 4 structures in this way is difficult for technical reasons and limits the rate of scientific progress in the life sciences. Hence, a computational method to split apart (decompose) superimposed biological structures acquired in a single image channel, i.e. without temporal multiplexing, would have tremendous impact. Here we present μ Split, a dedicated approach for trained image decomposition. We find that best results using regular deep architectures is achieved when large image patches are used during training, making memory consumption the limiting factor to further improving performance. We therefore introduce lateral contextualization (LC), a memory efficient way to train deep networks that operate well on small input patches. In later layers, additional image context is fed at adequately lowered resolution. We integrate LC with HIERARCHICAL AUTOENCODERS and HIERARCHICAL VAES. For the latter, we also present a modified ELBO loss and show that it enables sound VAE training. We apply μ Split to five decomposition tasks, one on a synthetic dataset, four others derived from two real microscopy datasets. LC consistently achieves SOTA results, while simultaneously requiring considerably less GPU memory than competing architectures not using LC. When introducing LC, results obtained with the above-mentioned vanilla architectures do on average improve by 2.36 dB (PSNR decibel), with individual improvements ranging from 0.9 to 3.4 dB.

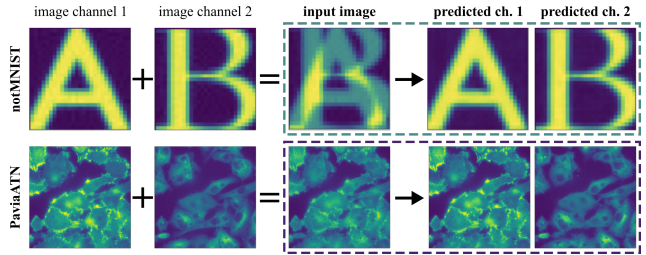


Figure 1. Splitting of superimposed image channels. The input image is the sum of two image channels, each channel containing structures from one given object class. The task of μ Split is to identify and split the structures superimposed in the given input image (dashed rectangles). We show examples from the *notMNIST* and *PaviaATN* datasets.

1. Introduction

Historically, image decomposition has found applications on natural images [1, 3, 8, 9]. Here we argue that a potentially impactful and unexplored application for image decomposition can be found in fluorescence microscopy.

Fluorescence light microscopy [10] is routinely used to look at living cells and biological tissues at sub-cellular resolution and is of utmost importance for virtually all research areas in the life sciences [17]. Fluorescence microscopy opens up windows to explore individual components of biological tissues and their constituting cells. This is achieved by highlighting cellular structures of interest with fluorescent labels, allowing the detailed investigation of those highlighted structures. Given the complexity of biological processes, it is typically desired to see how different cellular components relate to and/or interact with each other, requiring multiple fluorescently labeled components to be imaged within the same biological sample. This is enabled by using different fluorescent labels for different structures of interest, followed by time-multiplexed imaging of one label after the other [10] into so called image channels. Still,

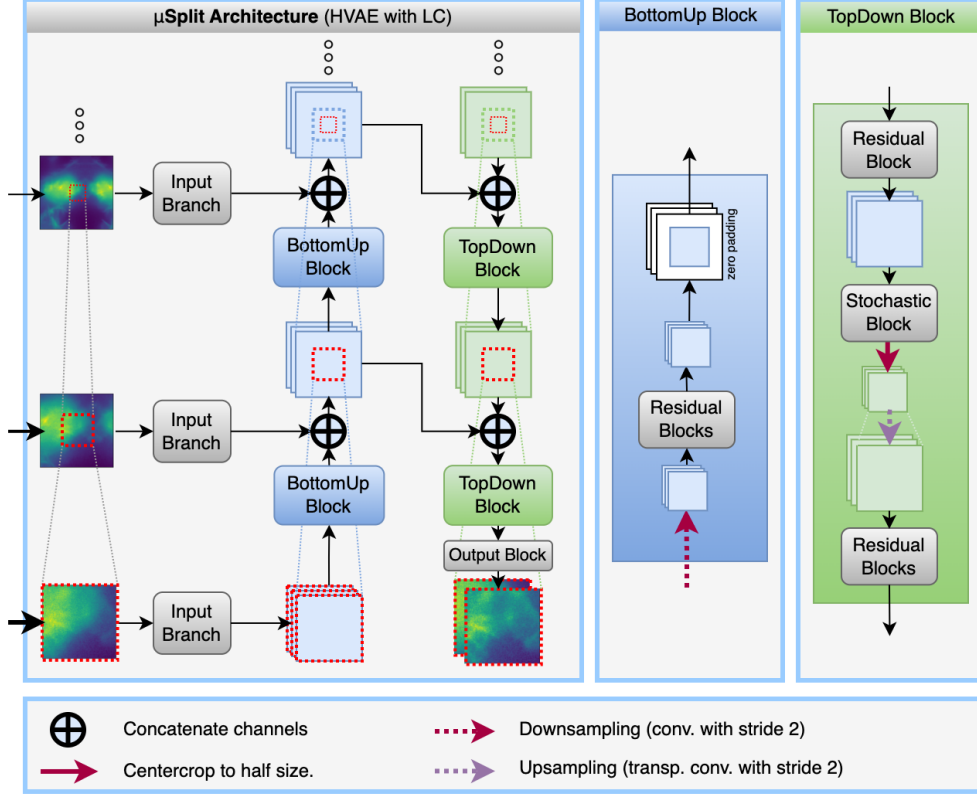


Figure 2. The network architecture of μ Split is based on either a HAE or HVAE [6, 24, 25]. By including lateral context, we are able to capture long range correlations in the data, while requiring only a fraction of the memory. The input (left side) consists of a core image patch, together with downsampled version of the patch surroundings – the lateral context. We show the area corresponding to the original patch as red dotted box throughout the figure. The original patch is fed to an *input branch* and then into a *BottomUp block*, where it is down-scaled and extended by zero padding to maintain the same pixel dimensions. The resulting tensor is concatenated with the down-scaled patch context. This process repeats at each hierarchy level of the HAE/HVAE using different level of lateral context. After the topmost level is reached, *TopDown blocks* merge the activation from the *BottomUp block* of each level with the activations generated by the next higher *TopDown block*. Each *TopDown block* crops the central region of the tensor and up-scales it, finally restoring the core patch to its original size.

imaging more than 3 or 4 fluorescent channels is difficult, because the emitted fluorescent light spectra start overlapping and can not well be separated any longer [10]. This is a major limitation of fluorescent light microscopy.

One way to circumvent this limitation would be to label two cellular components with the same fluorophore, *i.e.* image them in the same image channel. This makes image acquisition faster and cheaper and potentially leaves more room for additional components being imaged in other fluorescent channels. At the same time, it has the obvious downside that both biological structures labeled with the same fluorophore are now superimposed onto each other in one single image channel (see also Figure 1).

Here we present μ Split, a novel method to decompose superimposed images from a single image into separate image channels. This rests on the idea of learning structural priors for the two target image channels, and then

using these to guide the decomposition of the superimposed (added) pixel intensities. Such content-aware priors have previously been used for tasks such as image restoration [4, 26, 27], denoising [2, 11, 14, 15, 18, 19], and segmentation [5, 23, 28].

The achievable performance of many image processing tasks heavily depends on the portion of the image a network can see before having to make a prediction, *e.g.* receptive field and input patch size. With networks becoming deeper, receptive field sizes can start to grow larger than the largest patch size that can be used during training (due to GPU memory limitations). This requires to make interesting trade-offs between network architecture, patch size, batch size, and other factors determining GPU memory consumption. As we show in this work, the need for large spatial context, *i.e.* receptive field and patch size, is particularly pronounced for image decomposition tasks.

The idea of using additional spatial context has previously been used in the context of image segmentation [13, 16]. Leng *et al.* [16] devised a method to efficiently use the available context of the input image for the segmentation task. Hilbert *et al.* [13] worked with 3D images and used an additional lower resolution image to improve overall segmentation performance. Their work, though, did not generalize to using a hierarchy of lower resolution inputs.

Our main contributions are (i) proposing to use image decomposition in the context of fluorescent microscopy channel splitting, (ii) the creation of a synthetic *SinosoidalCrittters* dataset that distills the essence of the image decomposition problem at hand (see Section 4, (iii) the creation of a real fluorescent microscopy dataset (*PaviaATN*, see Section 4), (iv) proposing lateral contextualization (LC) and showing its superiority to all baseline methods, and finally (v) devising and evaluating a padding scheme enabling us to decompose large images avoiding tiling artefacts.

2. Problem Statement

A dataset $D_{mix} = (x^1, x^2, \dots, x^N)$ of N images is created by superimposing sampled pairs of image channels (D_1, D_2), such that

$$x^i = (d_1^i + d_2^i)/2, \forall i \in [1, N], \quad (1)$$

with $D_1 = (d_1^1, d_1^2, \dots, d_1^N)$ and $D_2 = (d_2^1, d_2^2, \dots, d_2^N)$.

Given an newly sampled $x = (d_1 + d_2)/2$, the task is to decompose x into estimates of d_1 and d_2 .

3. Our Approach

A Sound ELBO for μ Split. We train our VAE to describe the joint distribution for both channel images d_1 and d_2 . We modify the VAE’s ELBO objective to incorporate the fact that input and output are not the same (as they are for autoencoders). When training the VAE, our objective is to find

$$\arg \max_{\theta} \sum_{i=1}^N \log P(d_1^i, d_2^i; \theta),$$

based on our training examples (d_1^i, d_2^i) . Here, θ are the decoder parameters of our VAE, which define the distribution. Next, we expand $\log P(d_1, d_2; \theta)$ as

$$\begin{aligned} & \log \int P(d_1, d_2, z; \theta) dz \\ &= \log \int q(z|x; \phi) * \frac{P(d_1, d_2, z; \theta)}{q(z|x; \phi)} dz \\ &>= \int q(z|x; \phi) * \log \frac{P(d_1, d_2, z; \theta)}{q(z|x; \phi)} dz, \end{aligned} \quad (2)$$

where $q(z|x; \phi)$ is our encoder network with parameters ϕ . It can be shown that the evidence lower bound in Eq. 2 is equal to

$$E_{q(z|x; \phi)}[\log P(d_1, d_2|z; \theta)] - KL(q(z|x; \phi), P(z)).$$

By making the assumption of conditional independence of d_1 and d_2 given z , we can simplify the expression to

$$E_{q(z|x; \phi)}[\log P(d_1|z; \theta) + \log P(d_2|z; \theta)] - KL(q(z|x; \phi), P(z)). \quad (3)$$

Expression 3 is what we end up maximizing during training. Note that this analysis can be seamlessly extended to the case where one has a hierarchy of latent vectors [24] instead of just one.

For modelling $q(z|x; \phi)$, we use the identical setup of the bottom-up branch used in [19] with the input being x , the superimposed input. For modeling $P(d_1|z; \theta)$ and $P(d_2|z; \theta)$, we again use the top-down branch design used in [19] but make the top-down branch output two channels for mean and two more for the pixelwise $\log(\text{var})$, one each for d_1 and d_2 . So, the output of our model is a 4 channel tensor with identical spatial dimensions as the input.

Lateral Contextualisation (LC). Many popular architectures, such as U-NETS [22] or HVAEs [6, 19, 25] are composed of a hierarchy of levels that operate on increasingly downsampled and therefore also increasingly smaller layers. The basic idea of LC is to pad each downsampled layer by additional image context, *i.e.* additional input from an available larger input image, such that each layer at each hierarchy level maintains the same spatial dimensions. (In Figure 2, the red squares show where the original input patch lies within the downsampled inputs to other hierarchy levels and what additional context is added by LC.)

Creating downsampled LC inputs. Let $x_p = x_{[c, h]}$ denote a patch of size $h \times h$ from $x \in D_{mix}$ centered around pixel location c . To decompose the patch x_p , we additionally use a sequence of successively downsampled and cropped versions of x , $X_p^{\text{lowres}} = (x_{(p,1)}, x_{(p,2)}, \dots, x_{(p, n_{LC})})$, where $x_{(p,k)}$ is $x_{[c, 2^k \cdot h]}$, downsampled to the same pixel resolution of $h \times h$, and n_{LC} denotes the total number of used LC inputs (see Figure 2).

Implementation of μ Split. The implementation of μ Split is based on the implementation of HVAEs in [19]. The original input patch x_p is fed to the first input branch (IB). The output of this IB is fed to the first bottom up (BU) block, which downsamples the input via strided convolutions, whose output is then passed to some residual blocks (see supplement), and finally zero padded to regain the same spatial dimension as the input it received. The output of the first BU block is concatenated with the output of the second IB, which has received the first lower resolution input

containing additional lateral context, $x_{(p,1)}$. We use 1×1 -convolutions to merge these concatenated channels and feed the resulting layer into the next BU block. This procedure gets repeated for every hierarchy level in the given HVAE.

Once the topmost hierarchy level is reached, the last layer is fed into the topmost top down (TD) block. A TD block consist of some residual layers, followed by a stochastic block as they are used in HVAEs. The output of the stochastic block is center-cropped to half size and upsampled via transpose convolutions before again being fed through some residual layers (see supplement for details). Cropping and upsampling ensures that the output of the TD block matches the next lower hierarchy level. The output of the TD block is, similar to before, first concatenated with the output of the bottom up computations and then fed through 1×1 -convolutions.

Once we reach the the bottom hierarchy level, the output of the last TD block is fed through an output block (OB) composed of some additional convolutional layers, giving us the final predictions of d_1 and d_2 .

The one difference between HVAEs and HIERARCHICAL AUTOENCODERS (HAES) is that the stochastic block is replaced by the identity.

Variations of LC. Additional to the LC we described above, we experimented with two additional variations.

The first variation, *Lean-LC*, is the most memory efficient. We save memory by not using the lateral context introduced in the bottom up branch within the top-down branch (see supplementary figure). Specifically, the top-down branch reduces to the identical implementation as used in [19]. This is enabled by center cropping the bottom-up output layers to the required size of the corresponding top-down layer.

The second LC variation, *Deep-LC*, is motivated by the following observation. Hierarchical architectures lead to improved results, but the number of hierarchy levels is typically bounded by the initial input patch size¹. However, using LC, layers at each hierarchy level maintain the same spatial dimension and are therefore allowing more hierarchy levels to be added².

Here we added more hierarchy levels without adding more LC inputs. This means that starting from the highest hierarchy level using LC, any further level is exactly the same as in a regular HVAE.

Padding Strategies. Trained networks are often used to generate predictions for input images that cannot fit into available GPU memory. In such cases, the input image is typically cut into tiles and results are computed for each tile. Without suitable padding [22], the final tiled prediction will show artefacts at tile boundaries.

¹An input patch size of 2^k can at most yield k hierarchy levels.

²Only limited by the total image size, not the initial patch size

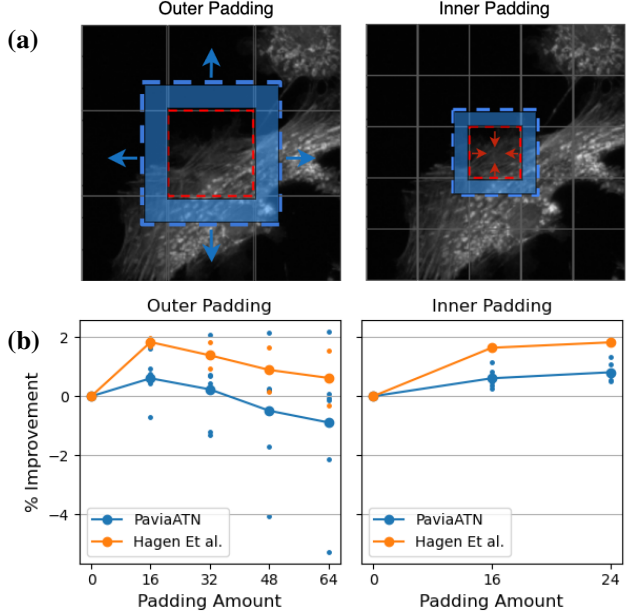


Figure 3. Outer vs. Inner Padding. (a) Outer padding, additional context (blue area) is added to training-patch-sized tiles and later discarded when tiling the full input image. This leads a different patch size during training and testing. In contrast, inner padding predicts on exactly training-patch-sized tiles, but only uses an inner core (red dashed square) to tile the input image, discarding the surrounding pixels (blue area). (b) Percentage variation in PSNR when using different amounts of outer or inner padding for vanilla HAE and HVAE architectures using an input patch size of 64. This amount denotes the number of pixels the blue box extends out of the red dashed square. For each amount of padding (x-axis), we plot 6 data points (two architectures, three tasks) for the *PaviaATN* data (blue) and 2 points for *Hagen et al.* dataset.

While regular padding, here referred to as Outer Padding, works well for networks trained on patch sizes that are at least as large as the networks receptive field (RF), we find ourselves in a regime where our patch size is typically much smaller then the largest RF of μ Split networks (see Section 5).

Whenever the patch size is smaller than the RF of a layer, its nodes are used to having most of their RF empty. Since outer padding enlarges the patch size fed to the network, larger portions of these receptive fields receive input³, leading to sub-par predictions. We quantify this in Figure 3(b).

Hence, better results can be achieved by keeping the fed input patch size constant, and instead of adding padded inputs to later discard, only use a center-cropped core of a predicted tile, as shown in Figure 3(a). Note that this will require a larger number of individual predictions, indicated by the smaller grid size seen in Figure 3 and further ex-

³These enlarged inputs are out-of-distribution w.r.t. the data used during training

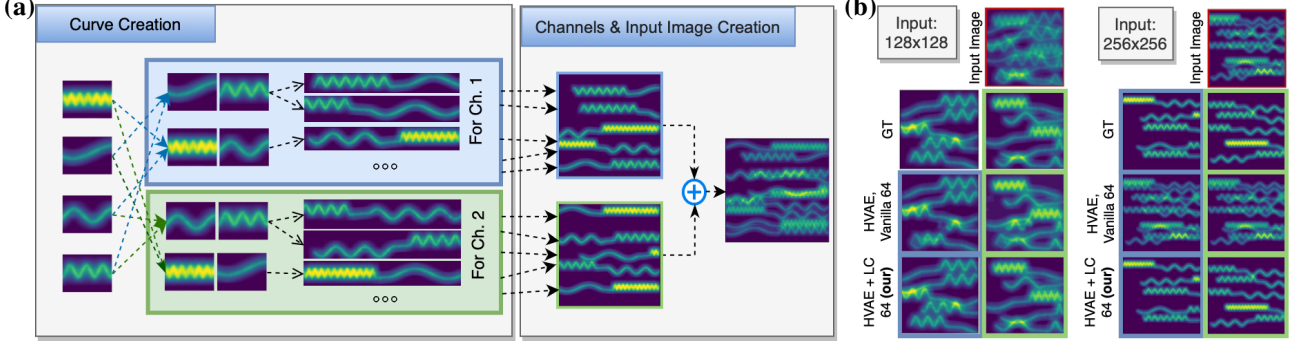


Figure 4. The synthetic *SinusoidalCrittters* dataset is designed so it can only be split by considering longer-range image context. **(a)** We first choose 4 different frequencies and combine them into 4 unique pairs. Two pairs are dedicated for image channel 1 (blue box), the other two for image channel 2 (green box). We call these pairs *critters*. The assignment of these critters to channels is done such that each frequency is assigned exactly once to each channel. We connect the two sinusoids of each critter with a low frequency curve of controllable length (later denoted by N_{join} in Table 1). Note that it is the specific combination of sinusoids present in the curve which decides whether it belongs to Channel 1 or 2 since the individual sinusoids themselves occur in both channels in equal amount. Next, we assemble channel images by placing a predefined number of randomly chosen curves at random positions in the respective image channel. The final input image is created as the sum of the two channels. **(b)** Two sample *SinusoidalCrittters* input images of size 128×128 and 256×256 pixels and the two channels that created them, respectively. Below, we show the decomposition results obtained with a trained vanilla HVAE with input patch size 64, and results obtained with the same architecture but using lateral contextualization (LC). To recognise which critter is depicted and assign it to a channel, the network has to see both wave forms. The vanilla HVAE is able to do splitting on 128×128 , but it has artefacts. For the 256×256 pixel images, it completely fails because it is unable distinguish between the critters since it cannot simultaneously process a sufficiently large part of the image. In contrast, by using LC we are able to successfully split both images.

plained in Section 5.

Training Details. For every dataset, we use 80%, 10% and 10% of the data as training, validation and test set, respectively. All models in this manuscript are trained using 16-bit precision on a Tesla V100 GPU. Unless otherwise mentioned, all models are trained with batch size of 32 and input patch size of 64.

For all HVAEs, we lower-bound σ s of $P(d_1, d_2, \theta)$ to $\exp(-5)$. This avoids numerical problems arising from these σ s going to zero, as reported in [21].

Next, we re-parameterize the normal distributions for the BU branch using σ_{ExpLin} reformulation introduced in [7]. We additionally upper-bound the input to σ_{ExpLin} to 20.

For training μSplit with *Deep-LC*, we follow the suggestions in [6, 20], and divide the output of each BU block by $\sqrt{2^i}$, with i being the index of the hierarchy level the BU block is part of.

4. Datasets

SinusoidalCrittters. We created this synthetic dataset to demonstrate the importance of context. A detailed sketch for how the dataset was created and an in-depth explanation can be found in Figure 4.

PaviaATN Microscopy Dataset. The *PaviaATN* dataset, imaged in the Synthetic Physiology Laboratory at the University of Pavia, is composed of 62 3-channel fluorescence microscopy images of size 2720×2720 . The three channels

Image Size	Model	$N_{\text{join}} = 0$		$N_{\text{join}} = 25$	
		PSNR	SSIM	PSNR	SSIM
128	Vanilla	28.3	0.88	25.5	0.84
	Lean-LC	37.3	0.97	35.1	0.95
	LC	37.0	0.97	39.2	0.98
256	Vanilla	19.4	0.73	15.8	0.4
	Lean-LC	34.1	0.97	32.2	0.96
	LC	41.5	0.99	41.6	0.98

Table 1. Quantitative results on the *SinusoidalCrittters* dataset. All results are reported in terms of peak signal-to-noise ratio (PSNR) and structural similarity index measure (SSIM). We compare results obtained with vanilla HVAEs that do not use lateral contextualization (LC), and HVAEs employing either Lean-LC or LC (*i.e.* μSplit results, see main text for details). All experiments are performed using a patch size of 64. Bold numbers denote the best result for any given task (columns), showing that our results consistently outperform the vanilla baselines.

label Actin, Tubulin and Nuclei, respectively, yielding three decomposition tasks we refer to as Actin vs. Tubulin, Actin vs. Nuclues, and Tubulin vs. Nucleus.

Hagen et al. Actin-Mitochondria Dataset. Here we used the highest resolution Mitochondria and Actin channels from the publicly available data provided by Hagen and colleagues [12].

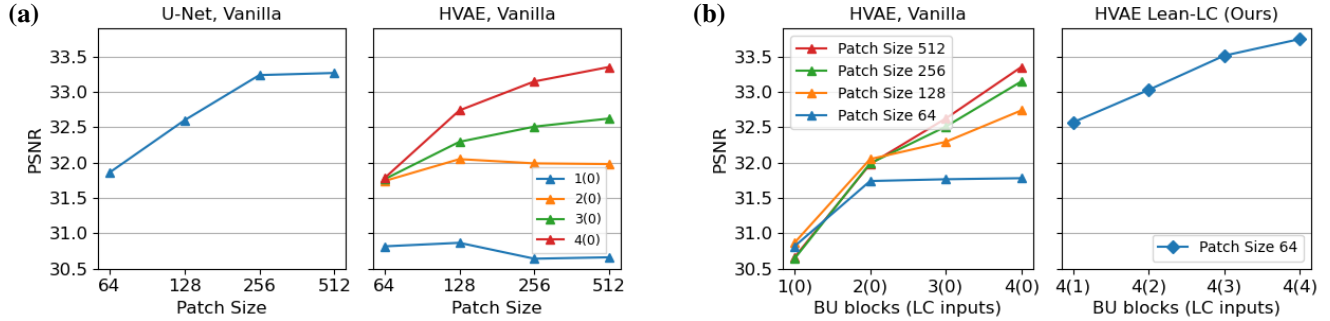


Figure 5. Quantitative results of baselines vs. μ Split (HVAE Lean-LC). (a) We plot the performance of the vanilla U-NET and the vanilla HVAE baseline trained on increasingly large patch sizes on the *PaviaATN* Act vs. Nuc data. The U-NET performance plateaus roughly at a patch size of about 256. The performance of the vanilla (not using LC) HVAE depends on how many hierarchy layers we use (1 to 4), but then also either plateaus or starts requiring a tremendous amount of GPU memory (see Table 2). (b) The left plot displays the same vanilla HVAE results but as a function of utilized hierarchy levels. Each curve plots the performance for a different patch size being used. The right plot, finally, shows results obtained with μ Split using an HVAE with patch size 64 and four hierarchy levels, but plotted as a function of how many of these levels, starting from the bottom-most one, use lateral contextualization (LC), indicated by the number in brackets. Not only does our approach outperform all other baselines (see also Table 2), it also requires only 4.4 GiB GPU memory, while the best performing vanilla HVAE requires 24.4 GiB.

Model + Patch Size		GPU (GiB)	PaviaATN						Hagen et al.	
			Act vs Nuc		Tub vs Nuc		Act vs Tub		Act vs Mit	
			PSNR	SSIM	PSNR	SSIM	PSNR	SSIM	PSNR	SSIM
Double-DIP		-	22.8	0.07	21.2	0.04	20.9	0.05	25.3	0.19
U-Net 256		9.4	33.2	0.61	31.4	0.56	28.1	0.58	34.2	0.88
U-Net 512		28.7	33.3	0.61	31.1	0.55	27.9	0.57	34.1	0.88
HAE	Vanilla 64	2.3	31.7	0.58	29.5	0.49	25.4	0.52	31.9	0.84
	Lean-LC 64	3.9	33.6	0.61	31.9	0.55	27.7	0.56	32.9	0.86
	LC 64	6.0	33.5	0.61	31.6	0.56	27.9	0.57	33.4	0.87
	Deep-LC 64	6.9	33.7	0.63	31.8	0.57	28.3	0.58	32.8	0.86
	Vanilla 512	31.2	33.2	0.61	30.2	0.53	27.6	0.56	34.2	0.88
HVAE	Vanilla 64	2.8	31.8	0.58	29.6	0.48	25.2	0.51	31.9	0.84
	Lean-LC 64	4.4	33.8	0.62	31.9	0.56	27.7	0.57	32.7	0.86
	LC 64	11.1	33.9	0.62	32.1	0.56	27.8	0.57	32.5	0.86
	Deep-LC 64	12.8	33.9	0.63	32.5	0.58	28.6	0.58	34.3	0.88
	Vanilla 512	24.4	33.4	0.61	32.9	0.54	27.6	0.56	34.3	0.87

Table 2. Quantitative results on fluorescent image decomposition tasks derived from the *PaviaATN* and *Hagen et al.* datasets. All results are reported in terms of peak signal-to-noise ratio (PSNR) and structural similarity index measure (SSIM). For each model we also report the used training patch size and GPU memory usage. The baselines we use are Double-DIP [9], U-NETS [22] trained on patch sizes 256 and 512, as well as vanilla HAEs and HVAEs using four hierarchy levels trained on patch sizes 64 and 512. The results of μ Split are also obtained with the same HAE and HVAE architectures trained on patches of size 64×64 , but with all hierarchy levels also employing either Lean-LC, LC, or Deep-LC (see main text for details). Bold numbers denote the best result for any given task (column). In all but one cases (*PaviaATN*, Tubulin vs. Nuclei), our results outperform all baselines despite having a comparatively lean memory footprint.

5. Experiments and Results

U-NET Hyperparameter Tuning. We tuned depth and patch size of a vanilla U-NET to achieve optimal performance for the tasks at hand (see supplement for details).

Effects of Larger Training Patch Sizes. In Figure 5(a) we show that increasing the training patch size improves the performance of a U-NET and vanilla HVAEs using different numbers of hierarchy layers. While the U-NET baseline

at some point stops improving with more image context being fed, HVAEs with sufficiently many hierarchy levels appear as if they could still improve, but quickly reach a hard limit in terms of GPU memory requirement (see Table 2).

Incrementally Introducing LC. In Figure 5(b) we show that μ Split allows us to further improve on all baselines performances, while at the same time reducing the required memory footprint (see Table 2).

This is enabled by working with small input patches of

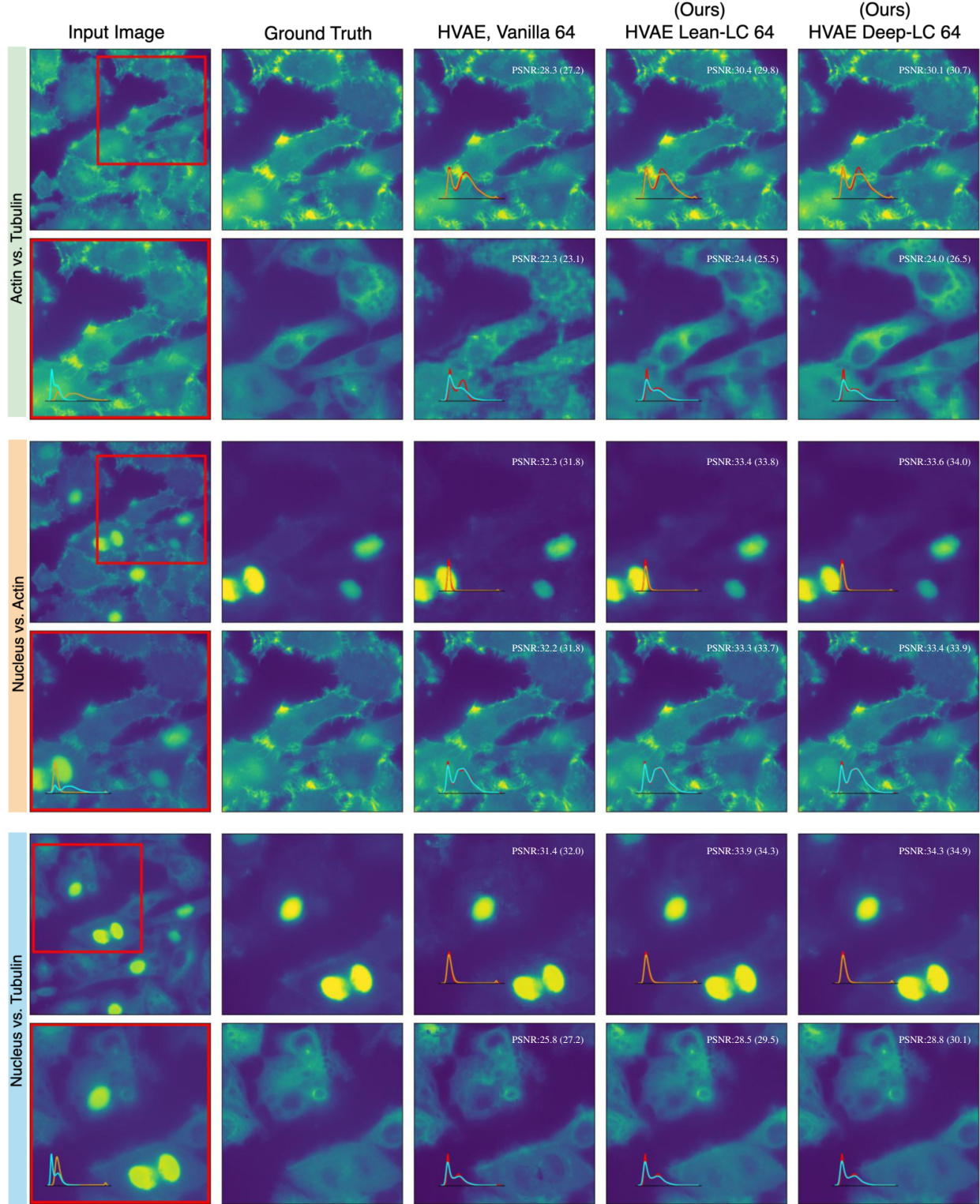


Figure 6. Quantitative results on the decomposition tasks derived from the *PaviaATN* dataset. We compare ground truth to results obtained with the vanilla HVAE baseline trained with a patch size of 64 to results obtained with two variations of μ Split (HVAEs using lean and deep LC, both also using a patch size of 64). The overlaid histograms shows either the intensity distribution of the two channels (column 1) or the intensity distribution of the ground truth and the prediction (red). The given PSNR are for the individual prediction (full input image) and for the entire dataset (in brackets).

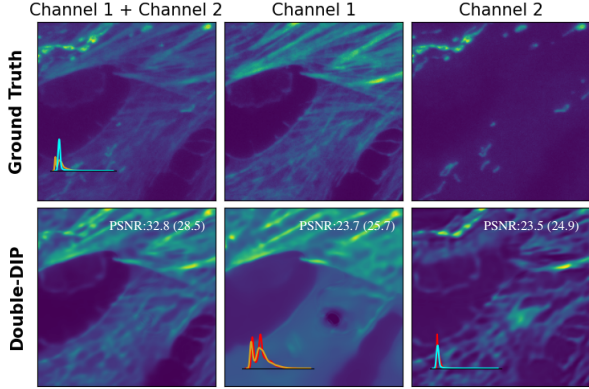


Figure 7. Qualitative image decomposition results using the Double-DIP baseline on an image of the *Hagen et al.* dataset. The overlaid histograms shows either the intensity distribution of the two channels (column 1) or the intensity distribution of the ground truth and the prediction (red). Note that Double-DIP is solving a much harder task since it is an unsupervised method trained on a single input images.

size 64 and introducing LC to an increasing number of hierarchy levels of the used HAE or HVAE. The number of hierarchy levels receiving LC input is denoted by the number in the brackets along the x-axis. Note that the vanilla HVAE with a input patch size of 64 quickly saturates in performance and does not benefit from additional hierarchy levels being introduced.

Experiments on Synthetic Data. In Table 1 we show the results obtained on the *SinoidalCritters* dataset. We used both input image sizes, 128×128 and 256×256 , and two values for N_{join} , namely 0 and 25 pixels, respectively. On average, μ Split outperforms the vanilla HVAE by 18 PSNR. Also note that the larger input size, constituting a harder problem to solve, is resulting in a drop of performance for the vanilla HVAE. Using μ Split, instead, the performance increases.

Experiments on Microscopy Data. We present results on 3 decomposition tasks on the *PaviaATN* dataset and 1 decomposition task on the *Hagen et al.* dataset. Table 2 summarizes our findings. We can see that all LC variants (*Lean-LC*, *LC* and *Deep-LC*) outperform the vanilla HAE and the vanilla HVAE using an input path size of 64 by at least one PSNR on all 4 tasks. Over all four tasks, the best performing LC variant with HVAE architecture outperforms the best LC variant with HAE architecture by 0.5 PSNR on average. Using the HVAE architecture, *Deep-LC* outperforms *Lean-LC* on average by 0.8 PSNR. For the HAE architecture this difference is 0.1 PSNR.

We have also applied the unsupervised Double-DIP [9] baseline to random sampled 6 crops of size 256×256 for each test-set image of the *PaviaATN* and *Hagen et al.*

datasets. Qualitative results are given in Figures 6 and 7.

Outer vs. inner padding and runtime performance. As can be seen in Figure 3(b, right plot), the vanilla HAE and vanilla HVAE setups perform better using inner padding. We used inner padding of 24 pixels, determined via a suitable grid-search.

Regarding the runtime performance during tiled prediction when using an inner padding of 24 pixels with a patch size of 64, we will end up using 16×16 center-crop per tile. Hence, we will need to predict 16 times more tiles to cover the entire input image.

Interestingly, we find that *Deep-LC* does not need any padding and all results reported for *Deep-LC* in Table 2 are computed without padding. This, in turn, leads to much improved runtimes for tiled predictions when using *Deep-LC*.

6. Discussion

In this work we show that μ Split performs better when deeper architectures, *i.e.* HAEs and HVAEs with more hierarchy levels, are employed. The deeper such networks become, the larger will the receptive field (RF) sizes grow, in our case routinely exceeding sizes of 512×512 pixels. At the same time, using such deep network architectures comes with tremendous demands on available GPU memory, forcing us to compromise on batch and patch sizes to be used during training. Still, when small patches are being fed, deep architectures cannot make use of their potentially large RFs, and trained systems will expect to see the entire, patch sized input. While this does not matter for tasks on fixed-sized inputs, when a trained fully convolutional network is later used on larger inputs, more of the RF gets utilized and we observe that the predictions deteriorate.

An immediate consequence of this observation is that we cannot employ common tiling schemes, which expect the RF to be smaller than the input patch size used during training. Hence, we propose to use inner tiling to circumvent this problem. Additionally we observe, that *Deep-LC* does not require any padded tiled predictions. The reason for this is likely that the patch context typically given by padding of tiles to be predicted is now fed via the deep lateral context sequence.

In summary, we propose a powerful new method to efficiently use image context. While we focus on a specific and potentially very impactful new image decomposition task on fluorescence microscopy data, we believe that the presented lateral contextualization ideas will help in the context of a wide array of other computer vision problems. In future work we will explore the applicability of lateral contextualization to other such problem domains, will make μ Split more amenable to noisy fluorescence data and will work on problems with more than two superimposed image channels.

Acknowledgements

This work was supported by compute infrastructure of the BMBF-funded de.NBI Cloud within the German Network for Bioinformatics Infrastructure (de.NBI) (031A532B, 031A533A, 031A533B, 031A534A, 031A535A, 031A537A, 031A537B, 031A537C, 031A537D, 031A538A). The authors also want to thank Damian Dalle Nogare of the Image Analysis Facility at Human Technopole for useful guidance and discussions and the IT and HPC teams for the compute infrastructure they make available to us.

References

- [1] Yuval Bahat and Michal Irani. Blind dehazing using internal patch recurrence. In *2016 IEEE International Conference on Computational Photography (ICCP)*, pages 1–9, May 2016. [1](#)
- [2] Joshua Batson and Loïc Royer. Noise2Self: Blind denoising by Self-Supervision. pages 1–16, Jan. 2019. [2](#)
- [3] Dana Berman, Tali Treibitz, and Shai Avidan. Non-local image dehazing. In *2016 IEEE Conference on Computer Vision and Pattern Recognition (CVPR)*, pages 1674–1682. IEEE, June 2016. [1](#)
- [4] Tim-Oliver Buchholz, Alexander Krull, Réza Shahidi, Gaia Pigino, Gáspár Jékely, and Florian Jug. Content-aware image restoration for electron microscopy. *Methods Cell Biol.*, 152:277–289, July 2019. [2](#)
- [5] Tim-Oliver Buchholz, Mangal Prakash, Deborah Schmidt, Alexander Krull, and Florian Jug. DenoiSeg: Joint denoising and segmentation. In *Computer Vision – ECCV 2020 Workshops*, pages 324–337. Springer International Publishing, 2020. [2](#)
- [6] Rewon Child. Very deep VAEs generalize autoregressive models and can outperform them on images. Nov. 2020. [2](#), [3](#), [5](#)
- [7] David Dehaene and Rémy Brossard. Re-parameterizing VAEs for stability. June 2021. [5](#), [S.2](#)
- [8] Tali Dekel, Michael Rubinstein, Ce Liu, and William T Freeman. On the effectiveness of visible watermarks, 2017. [1](#)
- [9] Yossi Gandelsman, Assaf Shocher, and Michal Irani. “Double-DIP” : Unsupervised image decomposition via coupled deep-image-priors, 2019. Accessed: 2022-2-14. [1](#), [6](#), [8](#)
- [10] Ionita C Ghiran. Introduction to fluorescence microscopy. *Methods Mol. Biol.*, 689:93–136, 2011. [1](#), [2](#)
- [11] Anna S Goncharova, Alf Honigmann, Florian Jug, and Alexander Krull. Improving blind spot denoising for microscopy. In *Computer Vision – ECCV 2020 Workshops*, pages 380–393. Springer International Publishing, 2020. [2](#)
- [12] Guy M Hagen, Justin Bendesky, Rosa Machado, Tram-Anh Nguyen, Tanmay Kumar, and Jonathan Ventura. Fluorescence microscopy datasets for training deep neural networks. *Gigascience*, 10(5), May 2021. [5](#)
- [13] Adam Hilbert, Vince I Madai, Ela M Akay, Orhun U Aydin, Jonas Behland, Jan Sobesky, Ivana Galinovic, Ahmed A Khalil, Abdel A Taha, Jens Wuerfel, Petr Dusek, Thoralf Niendorf, Jochen B Fiebach, Dietmar Frey, and Michelle Livne. BRAVE-NET: Fully automated arterial brain vessel segmentation in patients with cerebrovascular disease. *Front Artif Intell*, 3:552258, Sept. 2020. [3](#)
- [14] Alexander Krull, Tim-Oliver Buchholz, and Florian Jug. Noise2Void - learning denoising from single noisy images. *arXiv*, cs.CV:2129–2137, Nov. 2018. [2](#)
- [15] Alexander Krull, Tomas Vicar, Mangal Prakash, Manan Lalit, and Florian Jug. Probabilistic Noise2Void: Unsupervised Content-Aware denoising. *Frontiers in Computer Science*, 2:60, Feb. 2020. [2](#)
- [16] Jiaxu Leng, Ying Liu, Tianlin Zhang, Pei Quan, and Zhenyu Cui. Context-Aware U-Net for biomedical image segmentation. In *2018 IEEE International Conference on Bioinformatics and Biomedicine (BIBM)*. IEEE, Dec. 2018. [3](#)
- [17] Wei Ouyang, Fynn Beuttenmueller, Estibaliz Gómez-de Mariscal, Constantin Pape, Tom Burke, Carlos Garcia-López-de Haro, Craig Russell, Lucía Moya-Sans, Cristina de-la Torre-Gutiérrez, Deborah Schmidt, Dominik Kutra, Maksim Novikov, Martin Weigert, Uwe Schmidt, Peter Bankhead, Guillaume Jacquemet, Daniel Sage, Ricardo Henriques, Arrate Muñoz-Barrutia, Emma Lundberg, Florian Jug, and Anna Kreshuk. BioImage model zoo: A Community-Driven resource for accessible deep learning in BioImage analysis. June 2022. [1](#)
- [18] Mangal Prakash, Mauricio Delbracio, Peyman Milanfar, and Florian Jug. Interpretable unsupervised diversity denoising and artefact removal. Apr. 2021. [2](#)
- [19] Mangal Prakash, Alexander Krull, and Florian Jug. DivNoising: Diversity denoising with fully convolutional variational autoencoders. *ICLR 2020*, June 2020. [2](#), [3](#), [4](#), [S.2](#), [S.3](#), [S.4](#)
- [20] Alec Radford, Jeffrey Wu, Rewon Child, David Luan, Dario Amodei, Ilya Sutskever, and Others. Language models are unsupervised multitask learners. *OpenAI blog*, 1(8):9, 2019. [5](#)
- [21] Danilo Jimenez Rezende and Fabio Viola. Taming VAEs. Oct. 2018. [5](#)
- [22] Olaf Ronneberger, Philipp Fischer, and Thomas Brox. U-Net: Convolutional networks for biomedical image segmentation. In *Medical Image Computing and Computer-Assisted Intervention – MICCAI 2015*, volume 9351, pages 234–241. Springer International Publishing, Cham, Oct. 2015. [3](#), [4](#), [6](#)
- [23] Uwe Schmidt, Martin Weigert, Coleman Broadus, and Gene Myers. Cell detection with Star-Convex polygons. In *Medical Image Computing and Computer Assisted Intervention – MICCAI 2018*, pages 265–273. Springer International Publishing, 2018. [2](#)
- [24] Casper Kaae Sønderby, Tapani Raiko, Lars Maaløe, Søren Kaae Sønderby, and Ole Winther. Ladder variational autoencoders. *Adv. Neural Inf. Process. Syst.*, 29:3738–3746, Jan. 2016. [2](#), [3](#)
- [25] Arash Vahdat and Jan Kautz. NVAE: A deep hierarchical variational autoencoder. July 2020. [2](#), [3](#)
- [26] Martin Weigert, Loic Royer, Florian Jug, and Gene Myers. Isotropic reconstruction of 3D fluorescence microscopy images using convolutional neural networks. In *Medical Im-*

age Computing and Computer-Assisted Intervention - MIC-CAI 2017, pages 126–134. Springer International Publishing, 2017. [2](#)

- [27] Martin Weigert, Uwe Schmidt, Tobias Boothe, Andreas M uuml ller, Alexander Dibrov, Akanksha Jain, Benjamin Wilhelm, Deborah Schmidt, Coleman Broaddus, Siân Culley, Maurício Rocha-Martins, Fabián Segovia-Miranda, Caren Norden, Ricardo Henriques, Marino Zerial, Michele Solimena, Jochen Rink, Pavel Tomancak, Loïc Royer, Florian Jug, and Eugene W Myers. Content-aware image restoration: pushing the limits of fluorescence microscopy. *Nature Publishing Group*, 15(12):1090–1097, Dec. 2018. [2](#), [S.2](#)
- [28] Martin Weigert, Uwe Schmidt, Robert Haase, Ko Sugawara, and Gene Myers. Star-convex polyhedra for 3D object detection and segmentation in microscopy. *arXiv, cs.CV*, Aug. 2019. [2](#)

Supplementary Material

μ Split: efficient image decomposition for microscopy data

Ashesh¹, Alexander Krull², Moises Di Sante³,
Francesco Silvio Pasqualini³, Florian Jug¹

¹Jug Group, Fondazione Human Technopole, Milano, Italy, ²University of Birmingham, United Kingdom, ³ University of Pavia, Italy

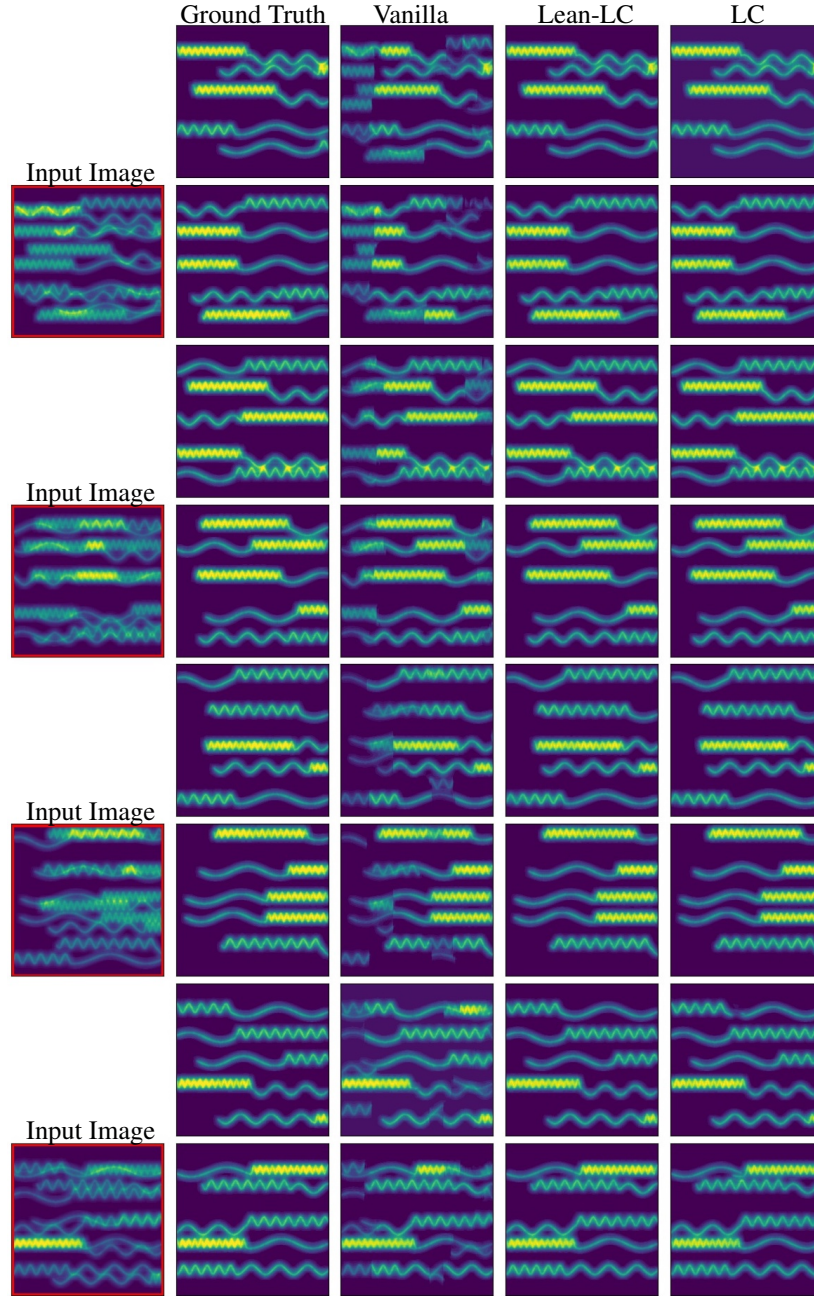


Figure S.1. Qualitative results obtained by different HVAE based architectures on 200×200 random crops of SinusoidalCrittters dataset inputs.

S.1. LC Architecture Variants

In this section, we describe the two LC variants: Lean-LC and Deep-LC. Lean-LC architecture is shown in Supplementary Figure S.2. Here, we use TopDown block from DivNoising[19]. The BottomUp block is identical to our LC architecture described in the main manuscript. The primary difference of Lean-LC compared from LC is that the output of TopDown blocks have different spatial resolution. The input to the top-most TopDown block has the smallest spatial resolution. The spatial resolution doubles with every next TopDown block. For example, if the input is of shape 64×64 , then in LC, output of every TopDown block has same spatial resolution, namely 64×64 . However, in Lean-LC, the output of all TopDown blocks have spatial resolutions smaller than 32×32 . It is therefore by design that it uses less GPU memory over LC.

Next, Deep-LC architecture is shown in Supplementary Figure S.3. Here, we simply stack the architecture proposed in [19] on top of our LC architecture. This allows the option of additional low-resolution latent spaces which are not possible in Vanilla HVAE. For example, if the input patch size is fixed to 64×64 , then Vanilla HVAE can have latent space on at most 5 resolution levels ($2^{5+1} = 64$). However, if we feed K LC inputs in the Deep-LC, then it can have at most $K + 5$ resolution levels. Note that in the LC architecture, the latent space always has the fixed spatial resolution, which is that of the input’s spatial resolution. This is what allows the Deep-LC to get more deeper.

S.2. Different Neural Network Submodules

Residual Block. We’ve taken the Residual block formulation from [19]. The schema for the residual block is shown in Supplementary Figure S.2 (b). The last layer in the residual block is the GatedLayer2D which doubles the number of channels through a convolutional layer, then use half the channels as gate for the other half.

Stochastic Block. The channels of the input of this block are divided into two equal groups. The first half is used as the mean for the gaussian distribution of the latent space. The second half is used to get the variance of this distribution, implemented via the σ_{ExpLin} reformulation introduced in [7].

S.3. Tuning U-Net for optimal performance

Here, we varied the depth by varying number of BottomUp (BU) blocks in the classic U-Net architecture. As seen in Table S.1, we see that performance starts to plateau at around 5 BottomUp blocks and so we’ve used U-Net configuration where BU Block is 5 in the main manuscript. Other relevant hyperparameter values used for its training are patience = 200 in EarlyStopping, patience =

BU Blocks	PSNR	SSIM
1	29.8	0.55
2	31.3	0.57
4	33.2	0.61
5	33.2	0.61
6	33.0	0.61

Table S.1. Performance variation of U-Net on increasing the number of BU blocks. In the main paper, we’ve used BU Block of depth 5.

30 in ReduceLROnPlateau (learning rate scheduler) and max_epochs = 400.

S.4. Metrics

We use PSNR and Structural similarity as the quantitative metrics. For PSNR, we use a variant that is invariant to arbitrary shifts and linear transformations in the ground-truth signal [27].

S.5. More Qualitative Results

Here, we show the performance on the splitting task on randomly chosen patches. In all figures shown in this section, each patch takes two rows: one row for one channel. The superimposed input region is shown in the first column. Next column has Ground truth channels and further columns have the splitting predictions from different model configurations.

S.5.1. Qualitative Results for Inner Padding

In Supplementary Figure S.4, we compare the Inner padding, Outer padding and the case when there is no padding on 400×400 sized random patches on Actin vs Nucleus splitting task. One can notice square patterns in the case when no padding is used. With inner padding, we see significant reduction in such patterns. With Outer padding, we see less of these patterns. However, with outer padding, we notice serious degradations specifically on bright regions spanning considerably large pixel space in the channel (row 1,3).

S.5.2. Splitting performance on random crops

In Supplementary Figures S.5, S.6, S.7 and S.8, we show performance of Vanilla HVAE, Lean-LC HVAE, LC HVAE and Deep-LC HVAE on 200×200 sized random crops. In Supplementary Figure S.1, we show the qualitative performance on random images of SinosoidalCrittters dataset.

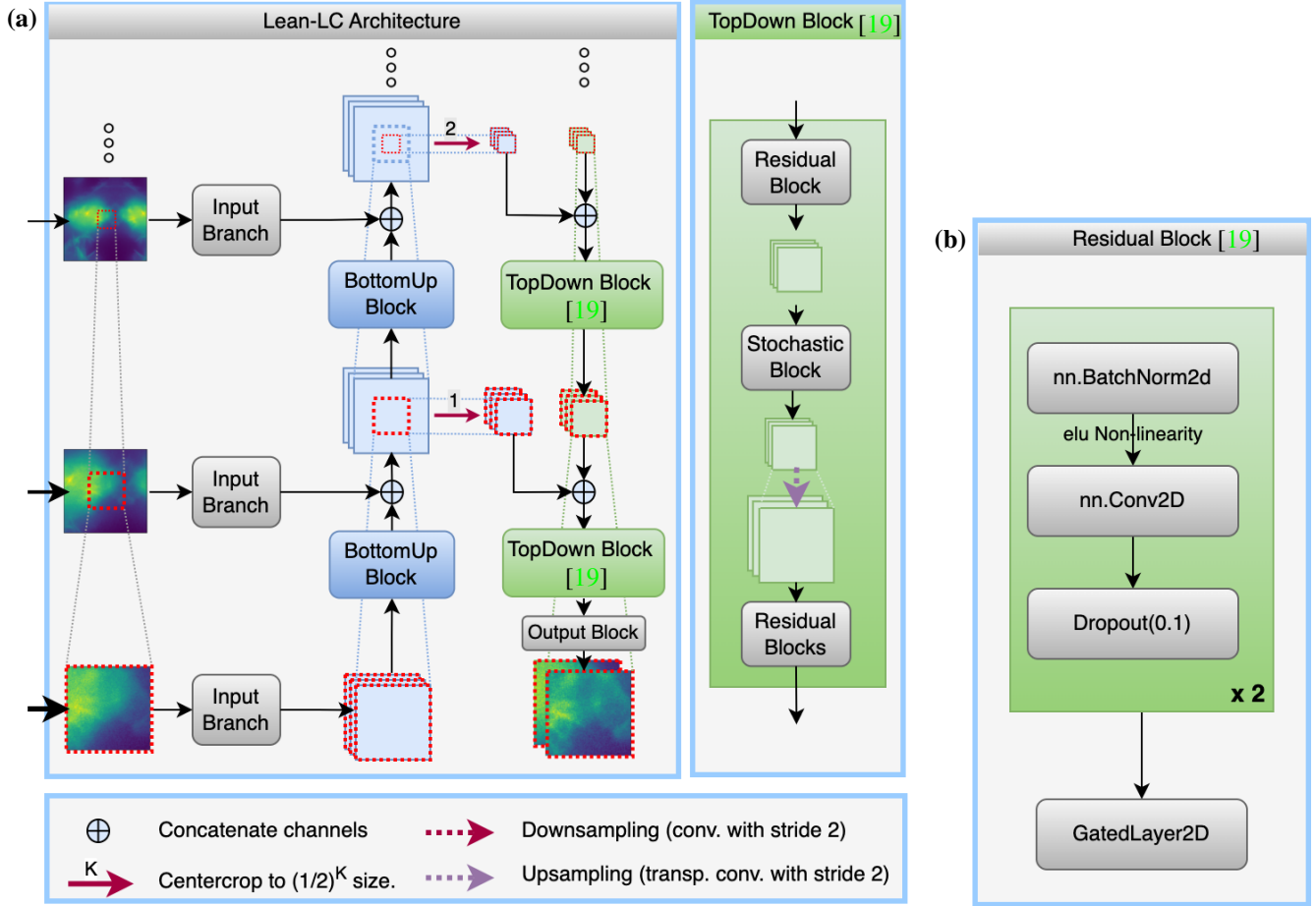


Figure S.2. **(a)** The network architecture of Lean-LC variant. The Bottom-Up block remains unchanged from the architecture of LC and it is Top-Down block which has changed. If we look at k^{th} Bottom-Up block (from bottom), then as before, the output from the k^{th} Bottom-Up block is passed to the next Bottom-Up block and also to the Top-Down block to the same level. However, before feeding to the Top-Down block, the output is center-cropped to $(1/2^k)^{th}$ size. The Top-Down block of LC-Lean is identical to the Top-Down block of /citePrakash2020-wr. Input to the block passes through Residual blocks and then through the stochastic block. The output of the Stochastic block is upsampled to twice its size through Transposed convolution with stride of 2. **(b)** The schema for the Residual Block. This is directly taken from [19].

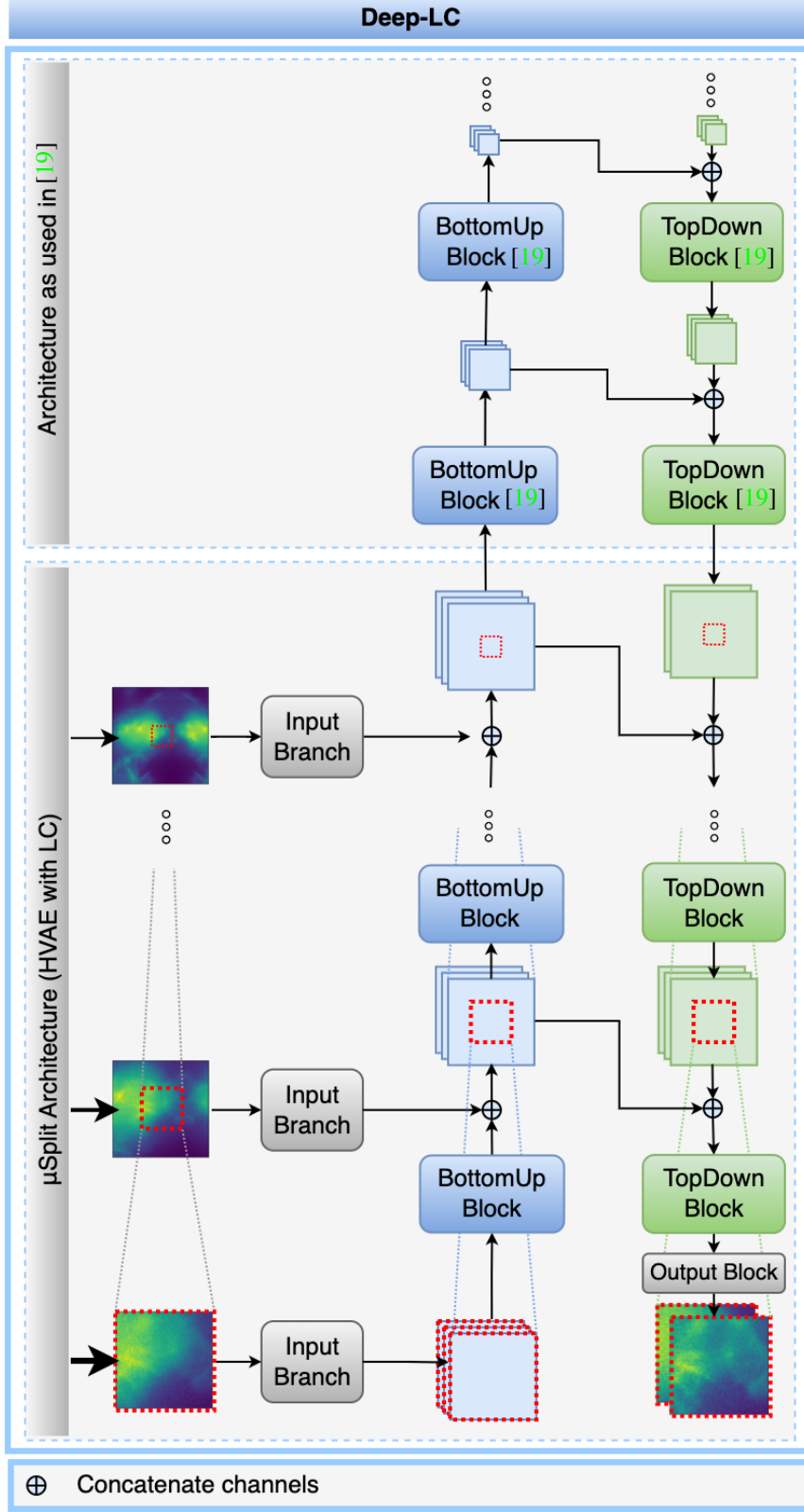


Figure S.3. The network architecture of our Deep-LC. Here, we stack the architecture used in [19] on top of our LC architecture. This effectively allows Deep-LC to work with much larger number of resolution levels than is possible with a vanilla HVAE setup. For example, if the input patch size is fixed to 64×64 , then Vanilla HVAE can have latent space on at most 5 resolution levels ($2^{5+1} = 64$). However, if we feed K LC inputs in the Deep-LC, then it can have at most $K + 5$ resolution levels.

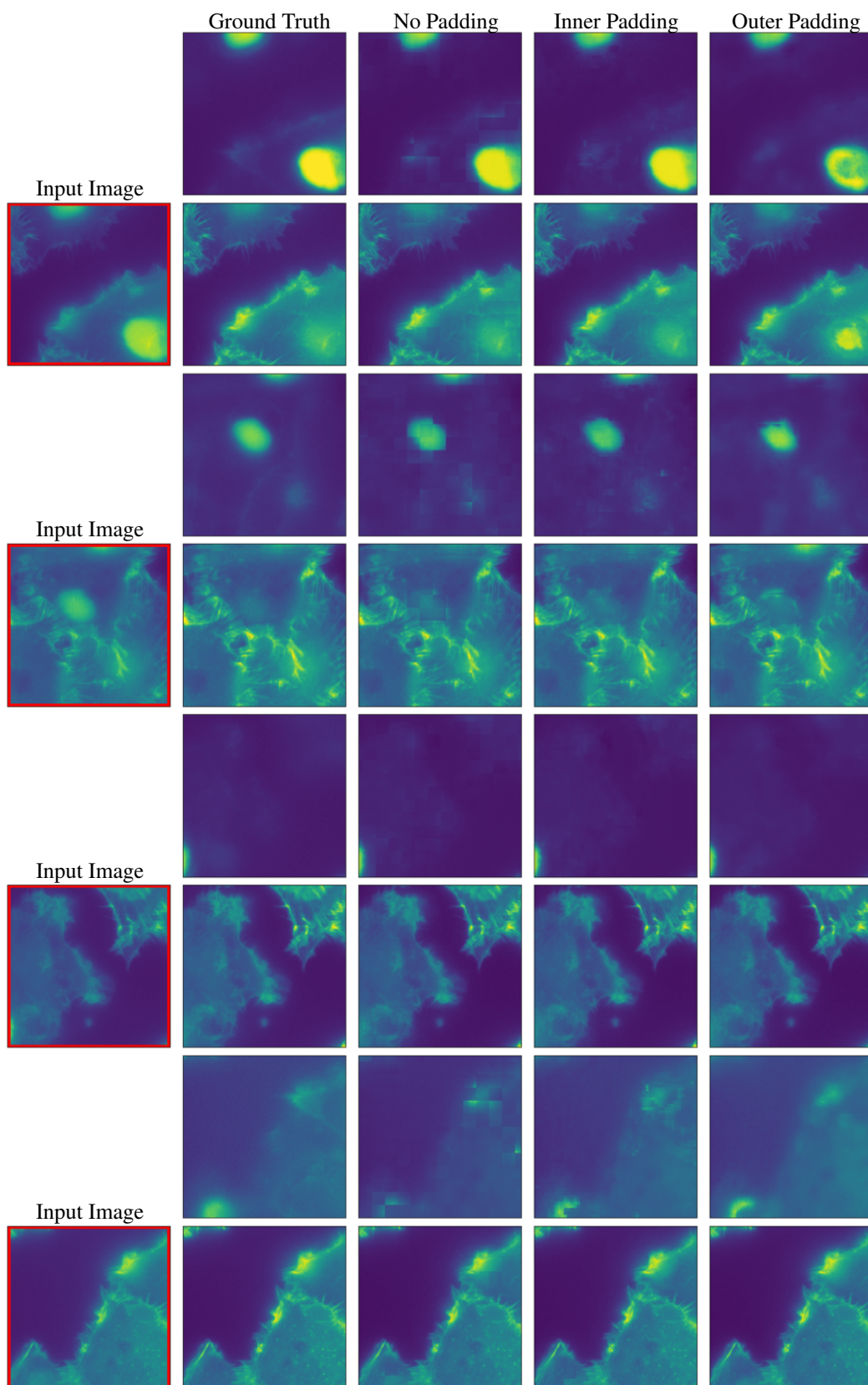


Figure S.4. Comparing *No Padding*, *Inner Padding* and *Outer Padding* on the Actin vs Nucleus task. One can see subtle but important differences obtained by the different architectures.

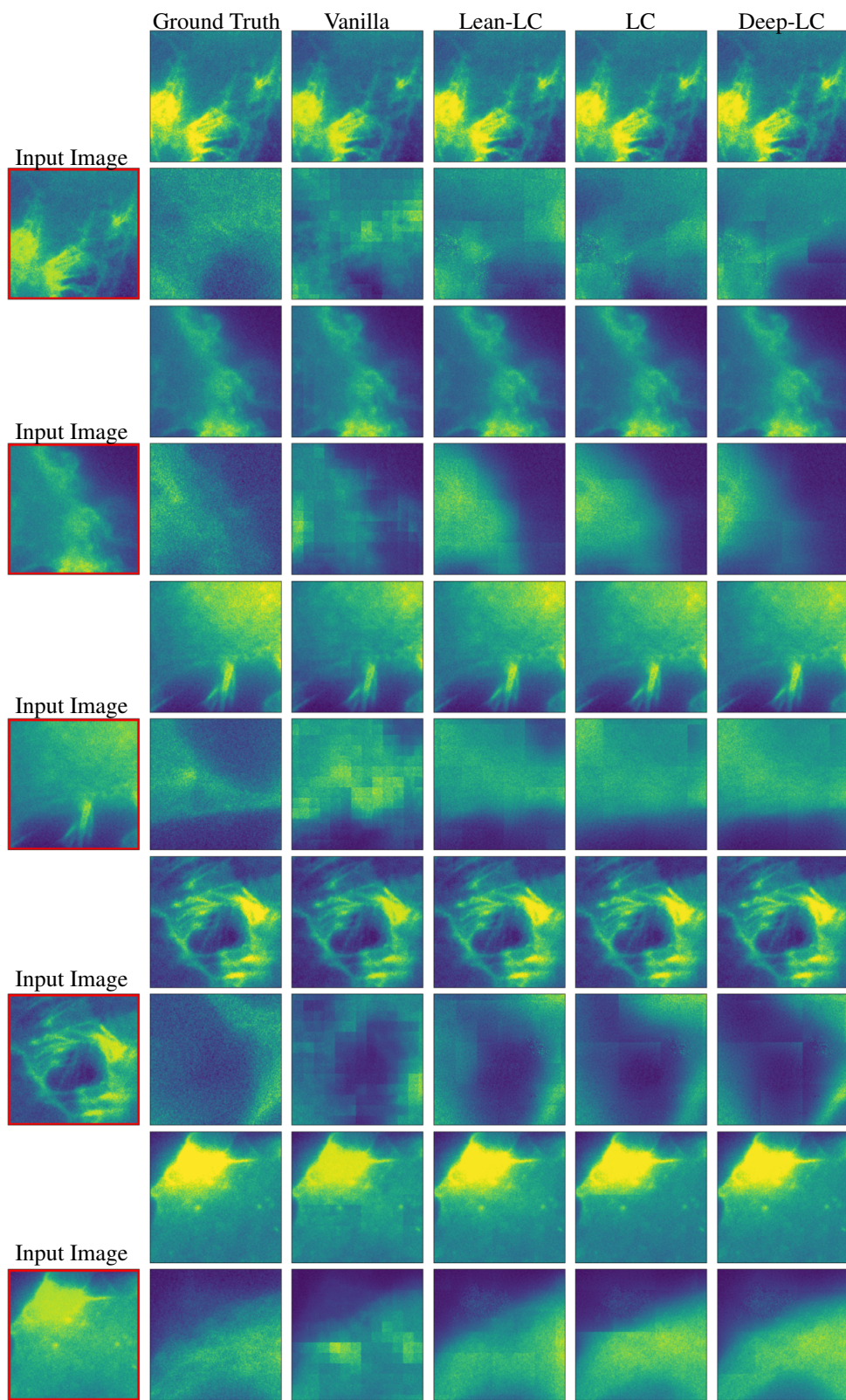


Figure S.5. Qualitative results obtained by different HVAE based architectures on 200×200 random crops of Actin vs Tubulin inputs.

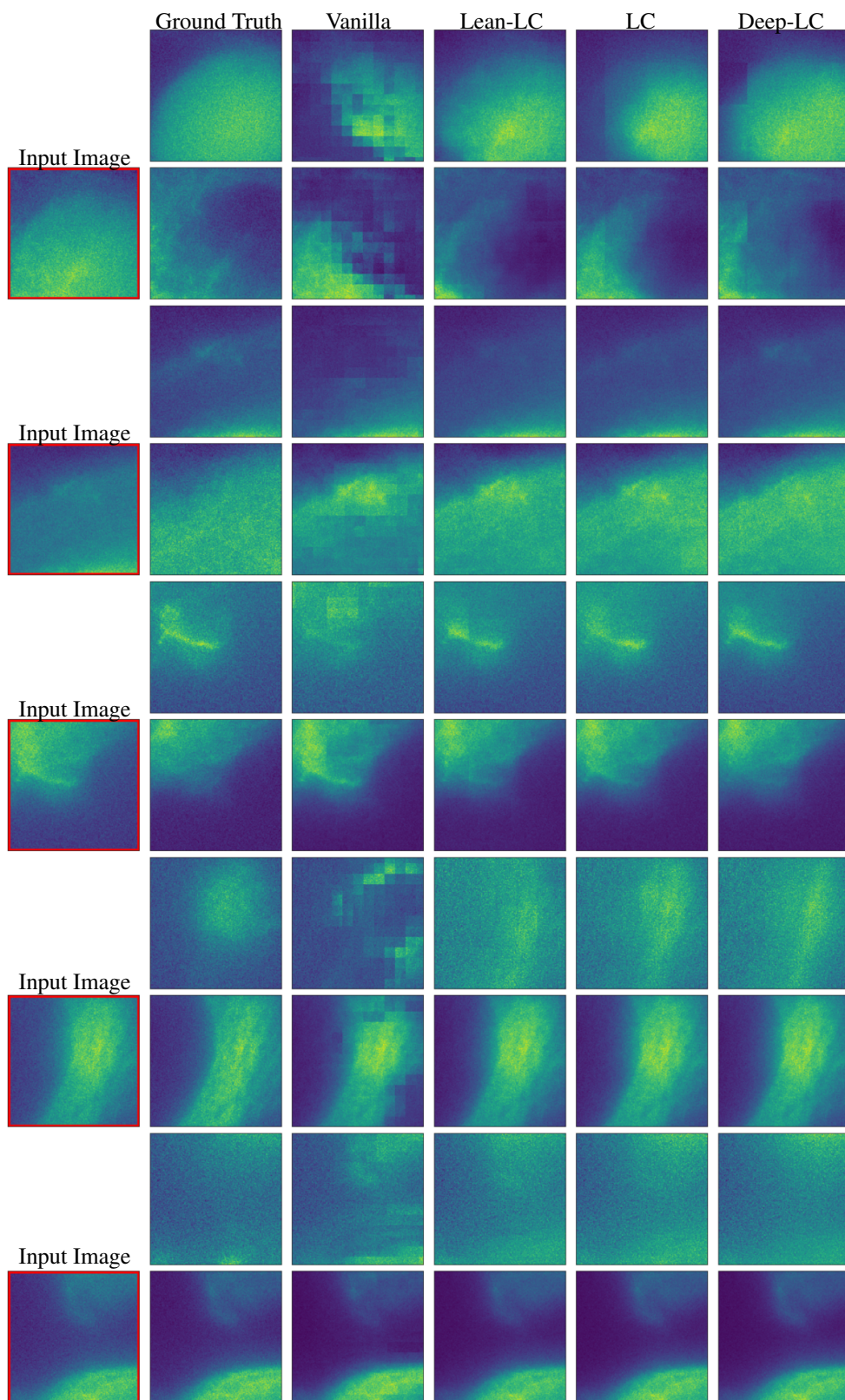


Figure S.6. Qualitative results obtained by different HVAE based architectures on 200×200 random crops of Tubulin vs Nucleus inputs.

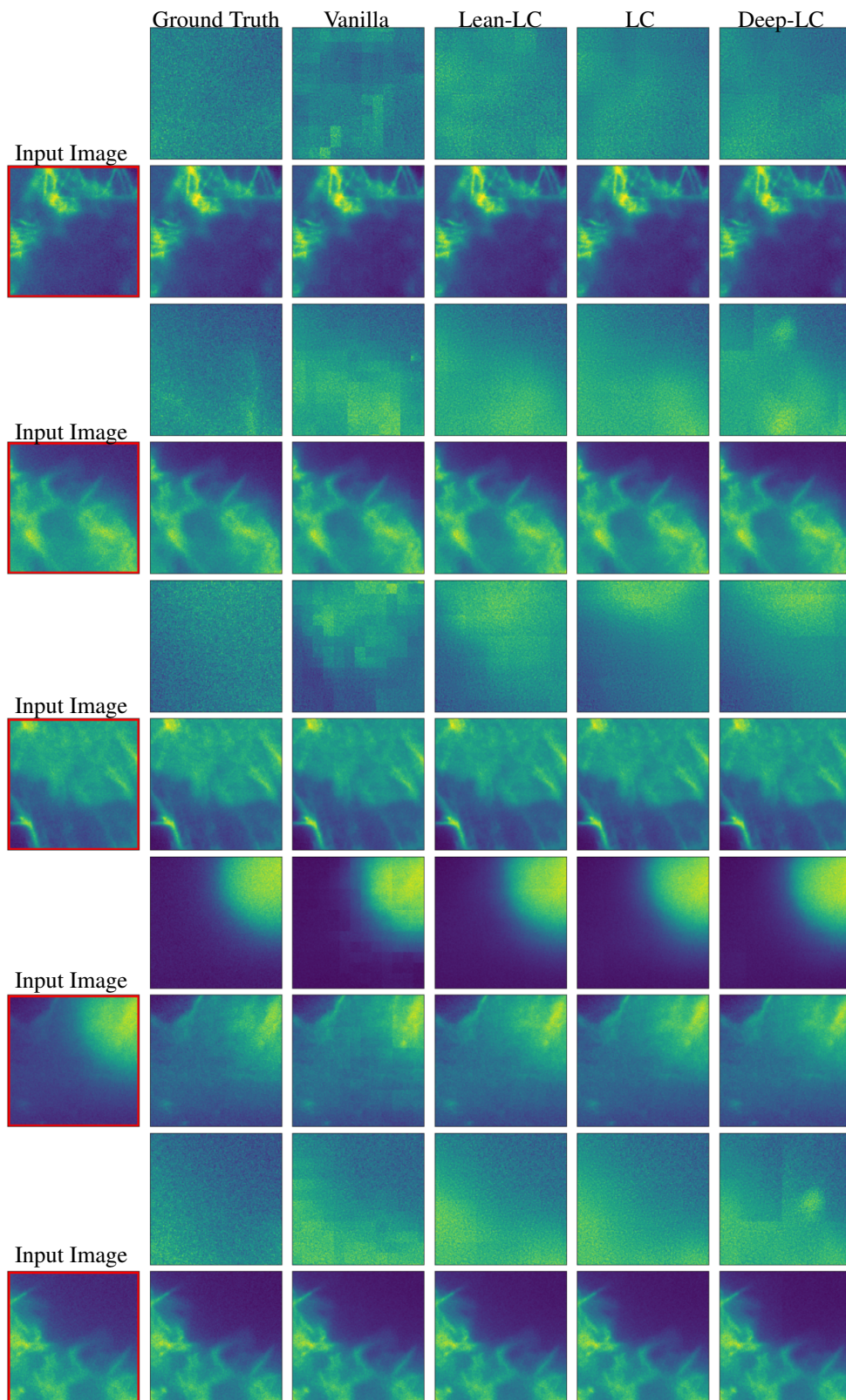


Figure S.7. Qualitative results obtained by different HVAE based architectures on 200×200 random crops of Actin vs Nucleus inputs.

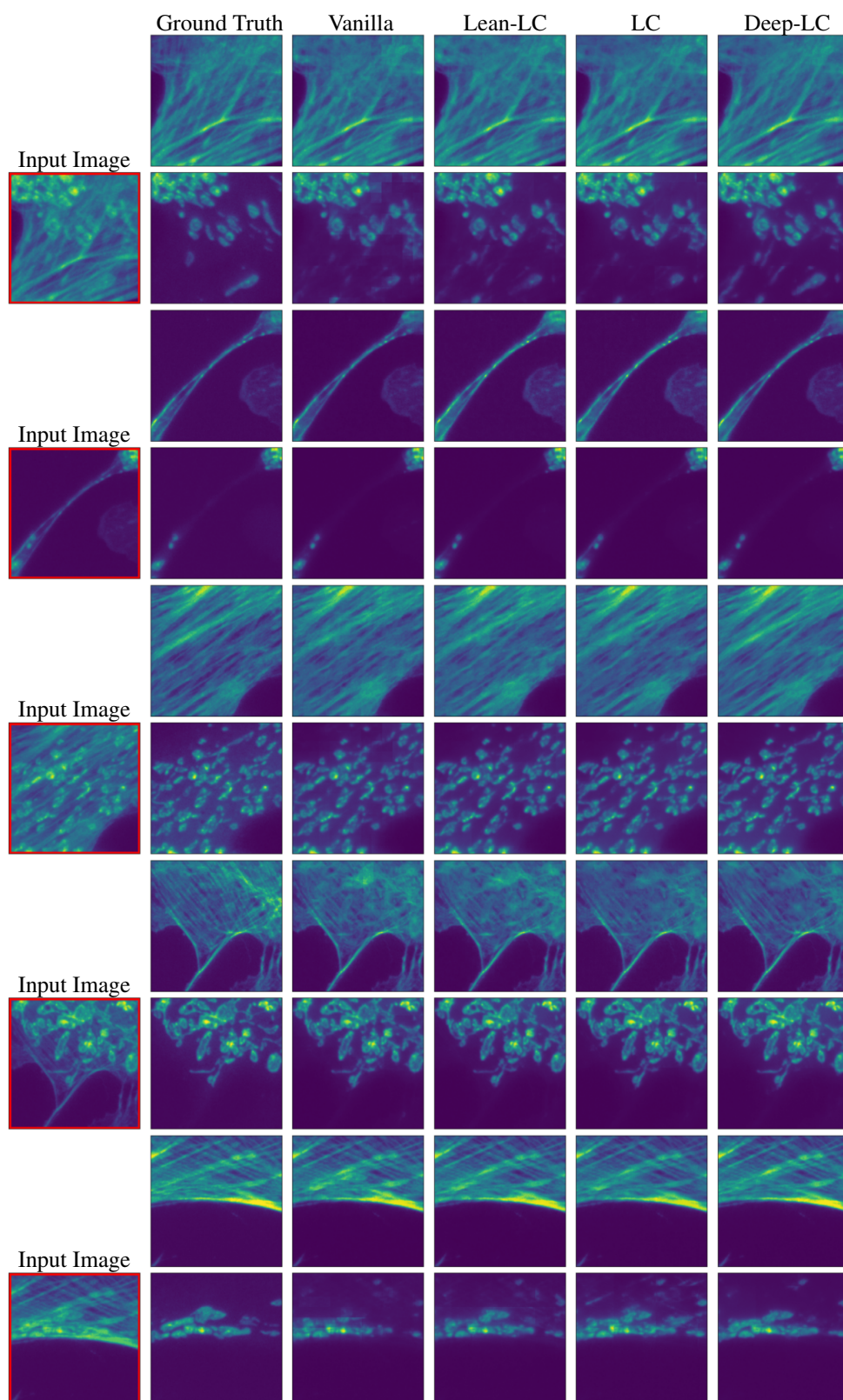


Figure S.8. Qualitative results obtained by different HVAE based architectures on 200×200 random crops of Actin vs Mitochondria inputs.